






Self-referencing for quasi shot-noise-limited widefield transient microscopy

MARTIN HÖRMANN,¹ FEDERICO VISENTIN,¹ 
SUMAN KUMAR CHAKRABORTY,² BISWAJEET NAYAK,²
PRASANA KUMAR SAHOO,² GIULIO CERULLO,^{1,3} 
AND FRANCO V. A. CAMARGO^{3,*} 

¹*Dipartimento di Fisica, Politecnico di Milano, Piazza L. da Vinci 32, 20133 Milano, Italy*

²*Materials Science Centre, Quantum Materials and Device Research Laboratory, Indian Institute of Technology Kharagpur, Kharagpur, 721302, West Bengal, India*

³*Istituto di Fotonica e Nanotecnologie - CNR, Piazza L. da Vinci 32, 20133 Milano, Italy*

**franco.camargo@cnr.it*

Abstract: Many applications of ultrafast and nonlinear optical microscopy require the measurement of small differential signals over large fields-of-view. Widefield configurations drastically reduce the acquisition time; however, they suffer from the low frame rates of two-dimensional detectors, which limit the modulation frequency, making the measurement sensitive to excess laser noise. Here we introduce a self-referenced detection configuration for widefield differential imaging. Employing regions of the field of view with no differential signal as references, we cancel probe fluctuations and increase the signal-to-noise ratio by an order of magnitude reaching noise levels only a few percent above the shot noise limit. We anticipate broad applicability of our method to transient absorption, stimulated Raman scattering and photothermal-infrared microscopies.

© 2024 Optica Publishing Group under the terms of the [Optica Open Access Publishing Agreement](#)

1. Introduction

Many applications of ultrafast optical spectroscopy and nonlinear optical microscopy require the measurement of small differential signals over large fields-of-view (FOV). Ultrafast transient absorption (TA) microscopy measures the absorption change of a delayed probe pulse following photoexcitation by an ultrashort pump pulse. As such, it enables the study of non-equilibrium phenomena with the combination of high temporal and spatial resolution and allows one to investigate the photoinduced dynamics of individual domains and nanostructures, as well as to visualize charge-carrier diffusion in real space and time [1–7]. Stimulated Raman scattering (SRS) microscopy uses synchronized pump and Stokes pulses at frequencies ω_p and ω_s , with detuning $\Omega = \omega_p - \omega_s$, resonant with a vibrational frequency of the sample, and measures the stimulated Raman gain(loss) of the Stokes(pump) pulse to quantify the density of vibrational oscillators at frequency Ω in the illuminated volume [8–10]. Photothermal infrared (PT-IR) microscopy employs an infrared pump pulse to directly deposit energy into a vibrational transition, and a visible probe pulse to measure the refractive index change due to localized heating that follows vibrational absorption [11–13]. The sensitivity to vibrational information provided by SRS and PT-IR makes these techniques important imaging tools for biochemical applications, such as histopathology for cancer detection [14], as it offers access to chemical information in a label-free fashion, unlike fluorescence microscopy.

All these experimental techniques require the detection of the small photoinduced differential transmission ($\Delta T/T$) of a probe pulse. To perform this measurement with high sensitivity, one must overcome shot-to-shot fluctuations in the probe pulse intensity to reach the ultimate shot noise limit, which in differential measurements is expressed as $(2/N)^{0.5}$, where N is the average number of photogenerated electrons on the detector per probe pulse (Ref. [15] or

section 2.3). Typically, laser systems display shot-to-shot energy fluctuations which limit the detection sensitivity. The relative intensity noise of a laser diverges for low modulation/detection frequencies (the so-called $1/f$ noise or excess laser noise) and decreases for increasing frequencies, reaching the shot noise limit in the best cases [16,17]. In the presence of excess laser noise, a so-called balanced detection configuration can be adopted, whereby a fraction of the probe beam is split off before interaction with the sample and recorded on a separate detector, to act as a reference. This independent measurement of the laser fluctuations can then be used to correct the signal [18–23]. Since the shot-noises of the reference and signal measurements are uncorrelated, the best results that can be achieved with this method remain above shot-noise by a factor of $2^{0.5}$ [18].

TA, SRS and PT-IR microscopy are typically performed in a point detection configuration, in which both pump and probe pulses are focused to diffraction-limited diameters and raster scanned across the sample. In this case, a single detector combined with a synchronous lock-in detection and high-frequency (hundreds of kHz to a few MHz) modulation of the pump beam can be employed [1,3], allowing one to approach, and in some cases reach, shot noise limited detection. Point detection architectures, however, require scanning of the focused pump/probe beams across the measured area, typically resulting in long acquisition times.

In widefield configurations, on the other hand, the probe pulse illuminates the whole FOV, and the illuminated sample area is relay imaged by a microscope objective combined with a tube lens to a two-dimensional detector, typically a CMOS camera [6,12,13,24]. The widefield approach allows parallel acquisition of the $\Delta T/T$ signal over all pixels of the detector, which has the potential to greatly reduce measurement times [24], and enables interferometric detection methods (e.g. holography). However, in standard implementations the modulation speed is limited by the camera's frame rate, setting the maximum pump beam modulation frequency as half the frame rate. The latter decreases as the number of pixels increases and values from tens to hundreds of Hz are typically used. Such low modulation frequencies introduce excess laser noise in the data, which limits the sensitivity of standard widefield approaches.

Recently, some of the authors demonstrated a solution to this problem which employs multiplexed off-axis holography [25,26]. Therewith, an all-optical lock-in camera allows shot-to-shot demodulation at arbitrary camera frame rates and FOVs in a widefield configuration, albeit at the price of added experimental and data reconstruction complexity. Here we take inspiration from the previously mentioned balanced detection schemes in transient spectroscopy. However, instead of using a second detector, we propose a radically simplified method applicable to widefield differential imaging, which dramatically increases the detection sensitivity. The idea is simple but powerful: we ensure that there are regions in the FOV which give no $\Delta T/T$ signal, which we show how to obtain for arbitrary samples. We use these areas to measure the intensity fluctuations of the probe pulses and remove them from the data. Thus, no copy or duplicate of the probe pulse is necessary, which makes the proposed method more robust. We demonstrate that this approach can lead to a signal-to-noise ratio (SNR) increase by a factor of ten in widefield TA microscopy and detection noise below the $2^{0.5}$ shot noise floor of typical balanced detection schemes [18]. Due to its generality and simplicity, we anticipate broad applicability of this method to TA, SRS and PT-IR microscopies.

2. Methods

First, we introduce the experimental setup of our widefield TA microscope and discuss the implementation of self-referencing. We then analyze the different contributions to the noise of the measurement and retrieve the theoretical noise floor.

2.1. Experimental setup

Figure 1(a) shows the experimental setup of our widefield TA microscope. The system is driven by an amplified Ti:sapphire laser (Coherent Libra), generating 100-fs pulses at 2 kHz repetition rate and 800 nm wavelength. Pump pulses at 400 nm are obtained via second harmonic generation (SHG), while tunable probe pulses from 500 to 750 nm are generated by an optical parametric amplifier. The pump-probe delay is controlled by a mechanical delay stage, and the pump beam is modulated by a mechanical chopper. Pump and probe beams are non-collinearly focused on the sample. The FWHM diameter of the probe ranges from ≈ 100 to $200 \mu\text{m}$, depending on the dataset, while $80 \mu\text{m}$ is used for the pump. After the sample, the probe beam is relay imaged by a microscope objective (0.60 numerical aperture) and a tube lens from the sample plane onto the camera. A long-pass filter removes the pump light after the objective. The global shutter camera (Basler acA720-520um, 720×540 pixels) has a nominal full well capacity of 20.7×10^3 electrons per pixel and is synchronized to the laser. However, while the laser runs at 2 kHz, the maximum frame rate of the camera is limited to 500 Hz. Thus, the camera records four laser shots for every exposure event. The chopper frequency is set to 250 Hz so that camera exposures in the presence and absence of the pump pulses are alternated. To make the acquisition fast and keep the amount of recorded data low, we average multiple images. Thus, throughout this work, we refer to pump-on/-off images, which we call T_{ON} and T_{OFF} respectively, as the average of one hundred images with the excitation beam on and one hundred images with the excitation beam off, acquired in an alternating fashion at 500 Hz, for an overall acquisition time of 400 ms. Also, to keep the amount of data low, we bin four adjacent pixels, since the magnification is such that the real space on the sample corresponding to one pixel is much smaller than the diffraction limit. Thus, when we refer to a pixel in this article, we talk about the average of two-by-two pixels on the camera. Finally, we note that photoinduced transient changes are typically of one part in 10^3 or even less, so the raw images in Fig. 1(b) are almost indistinguishable from one another when represented at full scale: the signal becomes clear only when the difference is taken.

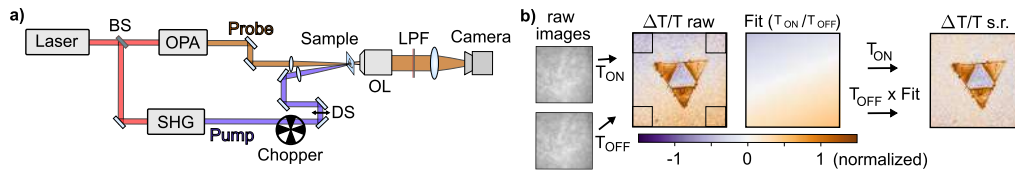


Fig. 1. a) Widefield TA microscope. BS: beam splitter, DS: delay stage, OL: objective lens, LPF: long-pass filter. OPA: optical parametric amplifier, SHG: second-harmonic generation b) Procedure for self-referencing. The raw images of the camera with (T_{ON}) and without (T_{OFF}) TA signal produce a normalized $\Delta T/T$ image of a lateral semiconductor heterostructure. Areas without signal (black rectangles in the corners) are used to fit a flat surface (Fit). This flat surface adjusts the T_{OFF} image, removing laser fluctuations in the self-referenced (s.r.) $\Delta T/T$ image (right).

2.2. Self-referencing scheme

The acquired images $T_{ON}(x, y)$ and $T_{OFF}(x, y)$ record the transmitted probe intensity as a function of position; for simplicity, in the following we drop the spatial dependence. In TA microscopy in the linear regime, the differential transmission signal is the pump-induced variation of the transmitted probe intensity and can be expressed as:

$$\frac{\Delta T}{T} = \frac{T_{ON} - T_{OFF}}{T_{OFF}} = \frac{T_{ON}}{T_{OFF}} - 1 = \Im\{\chi^{(3)}\}I_{pu}, \quad (1)$$

where I_{pu} is the pump intensity and $\Im\{\chi^{(3)}\}$ is the imaginary part of a complex-valued function of the pump and probe wavelengths as well as of the time delay between pump and probe pulses (for simplicity, we omit these functional dependences). From Eq. (1) it is immediately apparent that probe intensity fluctuations between the pump-on and pump-off acquisitions directly contaminate the measured signal and need to be averaged out.

To compensate for the intensity fluctuations of the probe pulse, we seek to measure them independently of the pump-induced differential signal. This is achieved by using areas of the widefield images in which no photoinduced signal is present, as shown in Fig. 1(b). Therein, a triangular sample, deposited on a transparent substrate which gives no transient signal, covers the FOV only partially. Hence, the probe intensity fluctuations in the presence and absence of the pump, which we refer to as $T_{\text{ref},ON}$ and $T_{\text{ref},OFF}$, can be measured independently from the TA signal on the sample-free areas. The transient signal can then be obtained applying the following averaging scheme (see Supplement 1 and Ref. [23] for details):

$$\frac{\Delta T}{T} = \frac{\langle T_{ON} \rangle}{\langle T_{OFF} T_{\text{ref},ON} / T_{\text{ref},OFF} \rangle} - 1 \quad (2)$$

In practice, the intensity noise in widefield images does not always appear as a uniform change over the entire FOV. Instead, for some acquisitions, we observe (non-systematic) gradients on top of a uniform change. For example, in Fig. 1(b), we observe that even outside the sample region the measured signal is non-zero. At the top it is positive, whereas it becomes gradually negative at the bottom. We attribute this effect to pointing jitter of the probe beam due to environmental factors. To take this spatial non-uniformity into account, we compute the mean values $\langle T_{ON} / T_{OFF} \rangle$ for selected points/areas (x, y) over the widefield image and fit a flat surface onto these points, for each acquisition. This retrieves the spatially dependent factor $T_{\text{ref},ON} / T_{\text{ref},OFF}$ in Eq. (2), by which T_{OFF} is then multiplied. The choice of a flat surface is empirical but has proven to work well. Figure 1(b) summarizes the procedure: areas without TA signal (black rectangles in $\Delta T/T$ raw) are selected to calculate a surface $T_{\text{ref},ON} / T_{\text{ref},OFF}$ (Fit), by which the T_{OFF} image is multiplied. The previous T_{ON} and rescaled T_{OFF} images are then used to calculate the self-referenced signal (Fig. 1(b) right).

2.3. Noise sources and noise floor

Next, we examine the detection noise achievable with self-referencing. In the unreferenced case, we retrieve a root mean square (rms) error of [15]:

$$\left(\frac{\Delta T}{T} \right)_{\text{RMS}} = \frac{1}{T} \sqrt{\langle \Delta T_{pr}^2 \rangle + 2 \langle \delta T_{SN}^2 \rangle + 2 \langle \delta T_{det}^2 \rangle}, \quad (3)$$

where $\delta T = T - \langle T \rangle$ is the deviation from a single pulse of the mean value $\langle T \rangle$. The first term $\langle \Delta T_{pr}^2 \rangle = \langle (T_{ON} - T_{OFF})^2 \rangle \approx 2\delta T_{pr} - 2\text{cov}(\delta T_{ON}, \delta T_{OFF})$ is the variance of the difference of the probe pulses T_{ON} and T_{OFF} and is the noise we want to remove with self-referencing. The second and third terms, $\langle \delta T_{SN}^2 \rangle$ and $\langle \delta T_{det}^2 \rangle$, are the variances of the shot noise and detector noise, respectively, of T_{ON} or T_{OFF} . These two noise sources are uncorrelated between acquisitions, which enables us to write the variance of the single detection events $\langle \delta T^2 \rangle$ in Eq. (3). Together, these two terms constitute the theoretically achievable noise floor of a detection system. As already mentioned, the shot noise is purely dependent on the number of collected electrons, whereas electronic noise summarizes all other noise sources (e.g. thermal/dark noise), which are independent of the signal level. If the full well capacity is mostly filled, which is a condition desirable in TA microscopy in order to minimize shot noise, then shot noise dominates over electronic noise [27,28]. To this end, it is important to protect the camera sensor from other light sources besides the probe pulses. Further, fixed pattern noise, which describes the static

performance of the individual pixels, is negligible due to the differential measurement scheme. Finally, care must be taken to prevent digital noise. In practice, the resolution of the bit depth, usually 8-, 10- or 12bit, should correspond to less collected electrons than the measured noise of the light pulses itself, thus avoiding that multiple readings are systematically rounded to the same integer value [1].

Next, to evaluate the specifics of self-referencing, we consider the case in which shot noise is the only noise source and N electrons are detected. Due to the Poisson distribution of shot noise, its variance $\langle \delta N^2 \rangle$ equals the average number of detected electrons $\langle N \rangle$. Since we are assuming that the electronic noise $\langle \delta T_{\text{det}}^2 \rangle$ is negligible, the rms noise floor in terms of detected electrons N is:

$$\left(\frac{\Delta T}{T} \right)_{\text{RMS, floor}} = \frac{1}{\langle N \rangle} \sqrt{2 \langle N \rangle} = \frac{\sqrt{2}}{\sqrt{\langle N \rangle}} = \sigma(N) \quad (4)$$

Note that here N corresponds to a single acquisition, e.g. either T_{ON} or T_{OFF} . Eq. (4) constitutes the absolute shot-noise limit of detection and would be the desired result for perfect referencing. However, as previously mentioned, while the reference contains the information of excess laser noise $\langle \Delta T_{\text{pr}}^2 \rangle$, it is itself an optical measurement and also contains shot noise σ_{ref} as in Eq. (4) (and detector noise) [15,18,29]. Moreover, the noises in the reference are uncorrelated to the corresponding noises in the image. Following [15] and assuming only shot noise, we retrieve for Eq. (2) the noise floor of the self-referenced signal:

$$\left(\frac{\Delta T}{T} \right)_{\text{RMS, floor, ref}} = \sqrt{\sigma^2(N_{\text{pr}}) + \sigma^2(N_{\text{ref}})} \quad (5)$$

with N_{pr} and N_{ref} the number of detected photons/electrons for the signal and referencing, respectively. Hence, the noise is always limited by the higher contribution in Eq. (5). Therefore, the shot noise introduced by the referencing process should be comparable or smaller than the noise of the desired signal, otherwise the referencing process can become detrimental. We also note that the well-known factor of $2^{0.5}$ in balanced detection schemes arises for an equal number of electrons/photons between signal and reference. Interestingly, in the context of our widefield implementation, the reference areas will generally outweigh the single pixels from the part of the image with signal. For instance, if features of $1 \mu\text{m}^2$ in a $50 \times 50 \mu\text{m}^2$ FOV are to be recorded with high signal-to-noise, and four areas of $9 \mu\text{m}^2$ at each corner are dedicated to self-referencing, then the detection noise is less than 1.4% above the shot noise limit for the $1 \mu\text{m}^2$ area of interest according to Eqs. (4) and (5). Therefore, performances beyond the often-mentioned $2^{0.5}$ limit above shot-noise are possible. Moreover, the area necessary for self-referencing ($4 \times 9 \mu\text{m}^2$) would be less than 1.5% of the FOV, so that the self-referencing operation does not appreciably reduce the information content of the widefield image.

However, self-referencing relies on points spatially distributed over the FOV. As such, in the case where a spatial dependence is present, for instance when there are pointing fluctuations, as in Fig. 1(b), the referencing area closest to a given point will account for most of the correction at that position. We conducted a numerical simulation to estimate this impact, by considering points for self-referencing at each corner, as in Fig. 1(b), which we believe is the most general choice. We find that the noise introduced by the self-referencing is smaller than the shot noise $\sigma^2(N_{\text{ref}})$ of a single corner over the entire FOV and approaches the shot noise of all four corners for points of interest near the center of the image (see Fig. S1 in Supplement 1).

Another aspect to consider is averaging over multiple acquisitions. Since the fluctuations of N_{av} individual acquisitions add up in a root-mean-square way, a decrease of the noise as $N_{\text{av}}^{-0.5}$ is obtained, regardless of whether referencing is used or not and which noise sources are present. Lastly, we note that pump pulse energy fluctuations are also present. However, this noise is proportional to $\mathfrak{I}\{\chi^{(3)}\}$ and thus of minor relevance with respect to the probe pulse fluctuations [15,19,29,30].

3. Experimental results

First, we analyze data without excitation pulses to verify and understand the effectiveness and limitations of the referencing approach. Then we demonstrate the referencing on two different cases: the special case in which the sample covers the FOV only partially, so that other parts of the image can be used for referencing, and the more general case for samples covering the entire FOV. In the following, when referring to shot noise we mean the noise of the probe without the noise introduced by the reference, unless stated otherwise.

3.1. Performance without sample

To verify the proposed referencing scheme and quantify its benefits, we first acquire and analyze data with the pump beam blocked and no sample present. Figure 2(a) shows a pair of recorded raw images. The full well capacity of the camera is filled at around 60%, indicating that the camera operates close to the shot noise limit [27,28]. We recorded more than 1000 pairs of T_{ON} and T_{OFF} images. For each of these pairs we calculate $\Delta T/T$, which is expected to be zero due to the absence of a pump. Some $\Delta T/T$ images are particularly noisy, due for instance dust in the air (Figure S2 in Supplement 1). To exclude those acquisitions, we prefilter the images prior to analysis by calculating the rms $\Delta T/T$ value for each image and remove all images for which it exceeds a given threshold. In this process, we remove nearly 5% of the $\Delta T/T$ images. Then, for the self-referencing we use 50×50 pixels in each corner (Fig. 2(b)), corresponding to a shot noise of 6.2×10^{-6} (considering pixels in all four corners). The self-referencing dramatically reduces the noise of the $\Delta T/T$ acquisitions, as shown in Fig. 2(c). To obtain a quantitative understanding of the effect of self-referencing, we separate the laser noise from shot noise by calculating the mean value over each $\Delta T/T$ image. Including the entire FOV leads to a large number of collected electrons, which reduces shot noise and makes excess laser noise dominant. The rms noise calculated over all acquisitions is 4.6×10^{-4} for the raw data and decreases by almost two orders of magnitude to 7.2×10^{-6} for the referenced data (Fig. 2(d)). Thus, we conclude that the excess laser noise in the acquired data is roughly the rms value of the mean value over the entire FOV of the raw data (4.6×10^{-4}). Considering that every image is integrated over 400 laser shots, this corresponds to a fluctuation of every four integrated probe pulses with their subsequent four probe pulses of 9.2×10^{-3} , in agreement with previous results [31].

Next, we analyze the noise in each pixel as a function of its signal. Figure 2(e) shows a scatter plot in which the density of pixel noise is plotted versus the total number of electrons recorded (signal, bottom horizontal axis) both for the raw and for the self-referenced data, while the top horizontal axis shows the corresponding camera counts in digital numbers (DN, 8-bit). The corresponding shot noise is also plotted as a dotted line. The self-referencing shifts the individual pixel noise towards their shot noise limit. The raw data noise matches with the shot noise of the individual pixels and the previously calculated laser noise when adding their squares as in Eq. (3). Figure 2(f) shows the effect of averaging multiple pixels together. The raw data saturates to the laser noise following Eq. (3), even for many averaged pixels when the shot noise becomes small. The self-referenced data at first matches the shot noise until, with increasing number of pixels, the shot noise of the reference starts to play an effect. The expected curve from Eq. (5), which includes the shot noise introduced by referencing, is also plotted, and we observe that the self-referenced data is slightly noisier than that. This small difference may be due to the fact that the noise introduced by the self-referencing is underestimated by not accounting for its spatial variances (Figure S1 in Supplement 1).

Lastly, we compare the noise reduction when averaging multiple acquisitions. To this end, we average a variable number N_{av} of subsequent acquisitions in our stack of roughly 1000 $\Delta T/T$ images prior to noise analysis. The starting values, which correspond to a single acquisition, are the same as in the previous plot in Fig. 2(f). With averaging, the noise decreases for the raw and self-referenced data with $N_{av}^{-0.5}$. For a single pixel, for which shot noise is comparatively

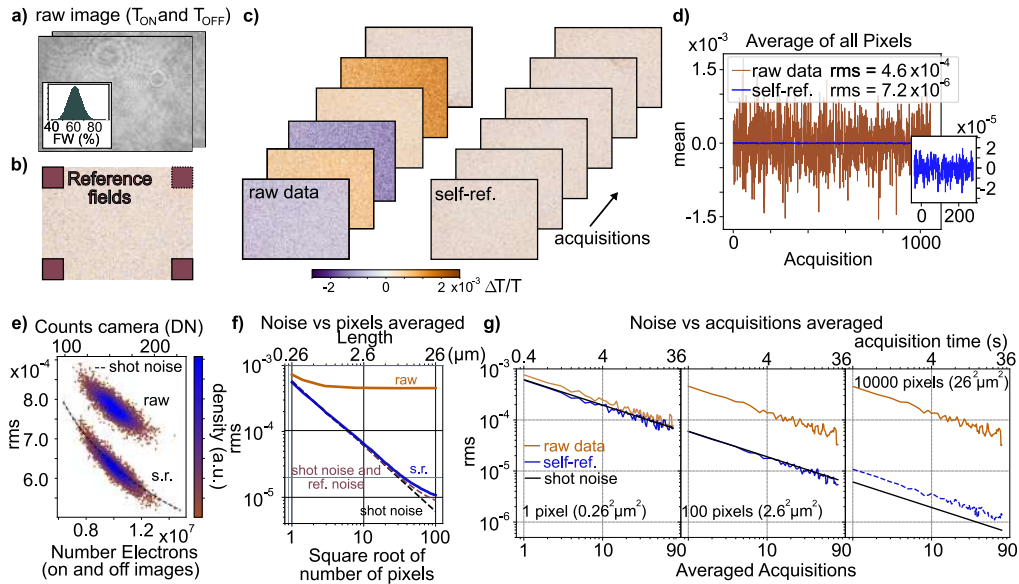


Fig. 2. Dataset with no excitation. a) Each $\Delta T/T$ image consists of two raw images. Inset: percentage of full well capacity filling of raw images. b) Areas (red) used for self-referencing. c) First few $\Delta T/T$ acquisitions without (raw data) and with referencing (self-ref.). d) Mean $\Delta T/T$ value over all pixels for raw data and self-referenced data versus acquisition. The values in the legend are rms over all acquisitions. Inset: self-referenced data 20 \times magnified. e) Density plot of noises (rms) of each individual pixel over time. The referencing sets the noise of the individual pixels to shot noise level. s.r.: self-referencing f) Noise (rms) when averaging multiple pixels together for raw data, self-referenced data, shot noise limit and expected noise (shot noise of signal and reference). g) Noise when averaging multiple acquisitions over time after averaging multiple pixels.

high, the difference between raw and self-referenced data is the same as in Fig. 2(e). However, when averaging 100 pixels together, the effect becomes more pronounced. The noise of the self-referenced data is a factor of 7.5 lower than that of the raw data and at the shot noise limit, whereas the raw data is limited by the laser noise. The same trend is observed when averaging even more pixels (Fig. 2(g) right-hand side). However, in this case, the noise of the self-referenced data exceeds the shot noise limit due to the shot noise introduced by the reference (Fig. 2(f)). Nonetheless, the self-referenced data's noise is a factor of 40 lower than that of the raw data.

3.2. Sample partially covering the FOV

Next, we apply our approach to TA microscopy, starting from a sample which only partially covers the FOV. We consider a lateral heterostructure of two monolayer semiconducting transition metal dichalcogenides (TMDs), MoS₂ and WS₂, at room temperature [32]. In two-dimensional materials such as TMDs, quantum confinement reduces the screening, which leads to strongly bound excitons below the quasi-particle bandgap [33]. In particular, the so-called A exciton peaks around 640 nm for MoS₂ and 600 nm for WS₂ (see Supplement 1). Figure 3(a) shows raw and self-referenced TA maps of a lateral heterostructure consisting of a central MoS₂ triangle with three WS₂ triangles attached. The nominal magnification used in this experiment is 72, so that each pixel corresponds to 191 nm. Due to the limited extension of the heterostructure on the FOV, the areas around the sample with no TA signal are used for self-referencing (rectangles in Fig. 3(a)). The 400 nm pump pulse, covering the entire FOV with a FWHM of 80 μ m, has

a photon energy well above the excitonic transitions of both materials. At the 600 nm probe wavelength, the WS₂ triangles display a positive signal (increased transmission) due to Pauli blocking of the A exciton transition [34], while the central MoS₂ triangle displays a negative signal due to bandgap renormalization of the B excitonic transition. The effect of self-referencing is highlighted in Fig. 3(b), which shows transient dynamics for three different points of the image: 1, corresponding to WS₂, with positive $\Delta T/T$ signal; 2, corresponding to MoS₂, with negative $\Delta T/T$ signal; 3, corresponding to the interface between the two materials. Each time trace is the average of 5×5 pixels, corresponding to an area of $0.92 \mu\text{m}^2$. For points 1 and 2 we observe bi-exponential decays, characteristic of excitonic relaxation in TMDs; for 3, we observe a completely different and more complex dynamics, potentially due to a mixed signal of both materials as well as charge carrier diffusion and interlayer hole transfer from MoS₂ to WS₂ [35].

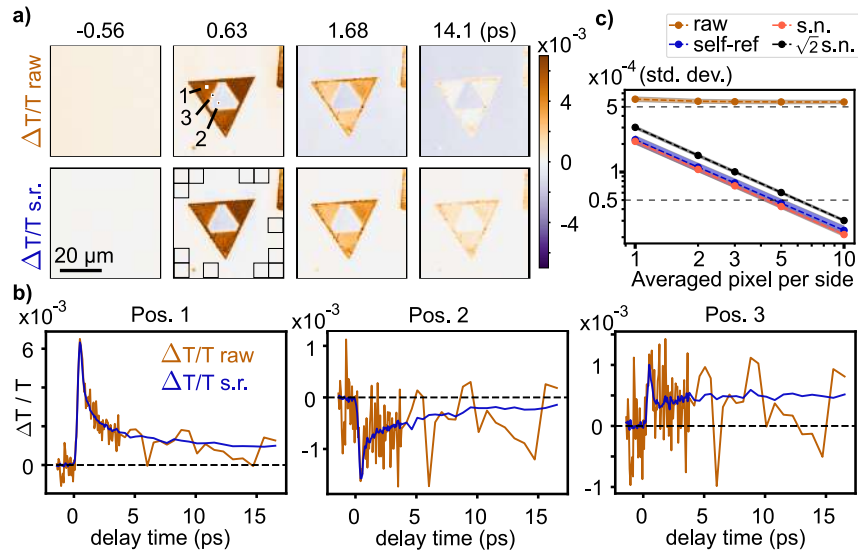


Fig. 3. TA images of a lateral heterostructure of monolayer MoS₂/WS₂ (MoS₂ in the centre) pumped at 400 nm and probed at 600 nm. a) $\Delta T/T$ images at different delays for raw and self-referenced (s.r.) data. The black rectangles show the area used for referencing. b) $\Delta T/T$ dynamics at selected positions of the image (numbered points in a). c) Noise statistics over the entire FOV at negative delay times for different number of averaged pixels. Shaded areas correspond to two standard deviations. s.n.: shot noise.

To obtain quantitative insight of the performance of self-referencing, we calculated the noise at negative delay times as a function of averaged pixels. To this end, the entire FOV is divided into $N \times N$ areas, with each area being the average of $n \times n$ pixels, with the pixels per side ranging from $n = 1$ to $n = 10$. For each of these areas the standard deviation over all negative time delays is calculated, in order to get a quantitative measurement of the noise. However, since only 18-time steps at negative delays are present, this standard deviation is calculated with the values of 2×2 adjacent averaged areas, in order to increase the sample size to 72, yielding a noise map with $N/2 \times N/2$ points. Figure 3(c) shows the mean value of all noises of the raw as well as the self-referenced data as a function of averaged pixels. Furthermore, their standard deviation is plotted to show the noise distribution over the FOV. The shot noise limit is calculated according to Eq. (4), whereas the number of collected electrons is retrieved from the individual images. As Fig. 3(c) shows, the self-referenced data is only slightly above the absolute shot noise limit and clearly below the noise floor of conventional balanced detection schemes, which is by a factor of $2^{0.5}$ above the shot noise limit. In contrast, the raw data remains at ca. 5×10^{-4} .

Table 1 shows the improvement of the self-referencing compared to the raw data. As uncertainty of the individual noise we used the confidence intervals, which are the standard deviation of Fig. 3(c) divided by the square root of the number of averaged areas $(N/2)^2$. For five pixels per side, corresponding to the areas used for the dynamics in Fig. 3(b), the noise decreases by a factor of 12.2.

Table 1. Self-referencing in Fig. 3

Pixel per side	Area (μm^2)	Raw / Self-ref.	Self-ref./shot noise
1	0.04	2.714 ± 0.002	1.0471 ± 0.0009
2	0.15	5.077 ± 0.009	1.065 ± 0.002
3	0.33	7.42 ± 0.02	1.082 ± 0.003
5	0.92	12.20 ± 0.05	1.092 ± 0.005
10	3.7	23.6 ± 0.2	1.12 ± 0.01

Regardless of the initial noise, self-referencing sets the noise almost to the shot noise limit. This is further confirmed by Table 1, showing the ratio of the noise of the self-referenced data to the shot noise limit. For the areas in Fig. 3(b), with five pixels per side, the noise is only 9.2% above the shot noise limit, to be compared with the 41.4% ($2^{0.5}$) above shot noise obtained in conventional balanced detection schemes. Importantly, self-referencing for these spatially confined samples does not require any modification of the experimental setup nor does it introduce additional computational complexity.

3.3. Sample fully covering the FOV

Next, we consider the more general case in which the sample fills the entire FOV. To perform self-referencing, we need to create excitation-free areas on the sample. Figure 4(a) shows our approach to this problem, with counter-propagating pump and probe beams. The FOV is $95 \times 71 \mu\text{m}^2$ with a pixel size of 265 nm. The objective lens and another lens relay-image a $600 \mu\text{m}$ round aperture onto the sample. The magnification is 0.15, giving a diameter of $90 \mu\text{m}$ on the sample. In this configuration a homogeneous pump illumination is achieved with the edges free from photoexcitation. Figure 4(b) shows the raw and self-referenced TA images of a large, spatially uniform WS_2 monolayer grown by chemical vapor deposition, pumped at 400 nm and probed at 620 nm, for an average of 10 scans. We observe a positive signal due to photobleaching of the A exciton, which displays the expected bi-exponential decay. In this experiment we found a weak TA signal also around the circular region corresponding to the image of the aperture, due to diffraction of the pump beam. Therefore, we referenced only at the corners, which are sufficiently distant to guarantee the absence of photoexcitation, using 20×20 pixels at each corner as referencing area. The $\Delta T/T$ signal in the images without referencing is fluctuating, as apparent in the background of the raw TA images. This fluctuation is removed by referencing, creating a continuous background shifted to zero.

Figure 4(c) shows dynamics of a $4 \times 4 \mu\text{m}^2$ area (black rectangle in Fig. 4(b)) for different excitation fluences and integration times. Particularly for low signals the self-referencing quickly retrieves small signals. Analogously to the analysis in Fig. 3, we divided the entire FOV into areas with the same dimension as used in Fig. 4(c) and calculated the noise via the standard deviation at negative delay times. Figure 4(d) shows the obtained noise levels for one and twenty averaged scans, and all three excitation fluences, together with their standard deviation and the expected shot noise levels according to Eq. (4). In this dataset, the noise improves by a factor of ca. 8 and is roughly 16% above shot noise limit, which is again less than with the conventional balanced detection (red error bars). This configuration makes self-referencing generally applicable and could be particularly useful for imaging of extended samples, such as, e.g., in chemometric

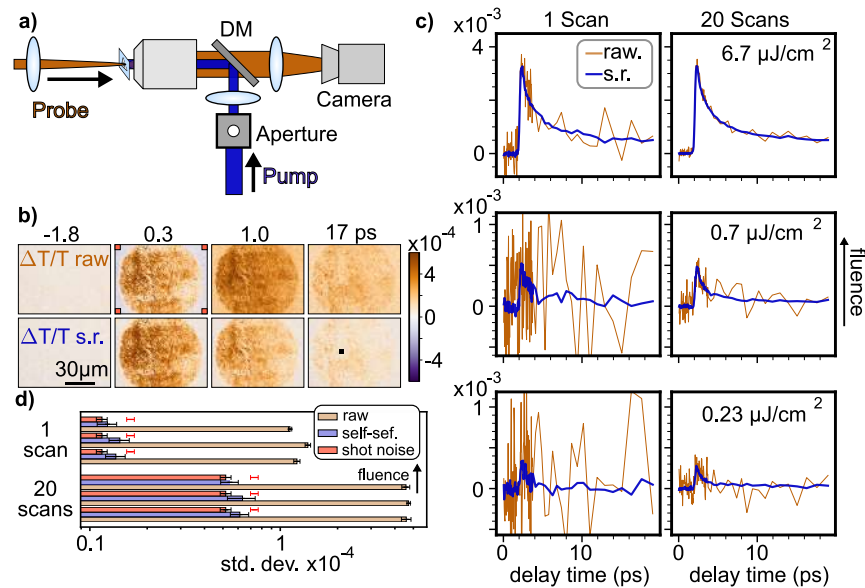


Fig. 4. Self-referencing for continuous samples. a) Imaging an aperture onto the plane of the sample in a 4f configuration creates a homogeneous round pump spot in the center of the image with pump-free edges used for self-referencing. DM: dichroic mirror. b) Raw and self-referenced (s.r.) TA images of a WS₂ monolayer, with pump at 400 nm and probe at 620 nm. Red squares show areas used for referencing. c) Raw and self-referenced TA dynamics for a $4 \times 4 \mu\text{m}^2$ spot (black rectangle in b) with different fluences and different number of averaged scans. d) Noise at negative delay times for areas used in c) over the entire FOV. Error bars correspond to one standard deviation. The red error bars show the shot noise multiplied by a factor of $2^{0.5}$.

imaging of tissue biopsies with SRS or PT-IR microscopy, or imaging charge carrier diffusion using pinhole arrays [26]. We note that there is nothing special about using a circular aperture and using the corners: any geometry that ensures sufficiently large signal-free areas to respect the points discussed in section 2.3 would result in an equally valid implementation of the method.

4. Discussion and conclusions

A few aspects of the method merit discussion. First, we note that the unreferenced and referenced images across all figures show very similar contrast, while the time-resolved kinetics of selected spatial coordinates show dramatic improvement after referencing (Figs. 3(b) and 4(c)). The reason behind this is related to the nature of excess laser noise in widefield imaging. All regions in the FOV are affected similarly by the fluctuation of the probe intensity with some slight variation, e.g. gradient in Fig. 1(b), accounted for by the fitting of a flat surface in the referencing process. Therefore, the main effect of probe intensity fluctuations on the data is not on the contrast of individual features on a given image, but on the image baseline. The self-referencing described here reliably measures and corrects for this baseline, leading to the clear kinetics obtained by stacking together different images. Moreover, it ensures that the quantitative signal level is accurately retrieved throughout the image. On the other hand, self-referencing seems at first glance less relevant for SRS and PT-IR microscopy, which do not aim to resolve TA kinetics but aim to retrieve images with high contrast. However, these methods seek chemical specificity and hence acquire images with different frequencies. In this process, self-referencing could greatly reduce noise, e.g. when implemented with Fourier transform spectroscopy [13]. Finally, it is

worth noting that the role of the mechanical chopper changes when self-referencing is used. Since the probe fluctuations are removed by the self-referencing process itself, the chopper is no longer necessary to minimize the probe pulse fluctuations via demodulating the signal shot-to-shot. Its remaining purpose is to allow the acquisition of T_{OFF} images. As such, in an ideal case of a static, non-degrading sample and no important drifts in experimental conditions, T_{OFF} images at negative times could be used and the chopper could be avoided, doubling the imaging speed.

In summary, we have developed an experimental method to remove excess laser noise of the probe beam in widefield TA microscopy. The method assumes that some regions of the sample FOV do not display a photoinduced signal, either because the sample is absent or because spatially confined excitation is used. These regions are exploited to acquire a reference signal which is used to cancel probe fluctuations in a self-referenced detection configuration. The measurement of the probe fluctuations on the same camera makes the method particularly robust, compared to common balanced detection schemes which measure a duplicate of the probe pulse on a second detector. The idea to measure the probe fluctuations on the same detector was also applied in spectroscopy, termed “edge-pixel referencing” [15,30,36], however, with different implications, as spectra are measured. In the context of widefield TA microscopy, it has been briefly mentioned in the case of diffraction-limited excitation with a small FOV [37]. Here, we have developed and characterized this method for any photoexcitation and sample condition. We demonstrate an improvement in the SNR of the TA data by one order of magnitude, bringing detection basically to the shot noise limit and below the noise floor of conventional balanced detection schemes ($2^{0.5} \times$ shot noise). The most important aspect of the method is that it removes the need to demodulate the differential signals at high frequencies. Thus, cameras in widefield configurations can run in the low frequency (≈ 100 Hz - 1 kHz) regime, in which laser noise is present, while still achieving close to shot noise-limited detection. Therefore, the presented method represents a continuation of previous setups [25,26], but with the advantages of (i) lower experimental complexity, (ii) broad applicability, due to its simplicity and (iii) a self-referenced detection scheme rather than shot-to-shot acquisition [25,26].

Hence, increasing signal to noise becomes a matter of collecting enough photons to reduce the shot noise. Therefore, we believe that widefield configurations will play an increasingly more significant role in the future, as the continuous progress in sensors and data transfer will allow the detection of more photons on the same time scales. Currently top-end camera sensors are able to detect over one hundred times more photons in the same time interval compared to the camera used in this work. This will increase the sensitivity, FOV, allow techniques such as holography and decrease experimental complexity. Therefore, we anticipate that our method will find applications in TA, SRS and PT-IR microscopy experiments.

Funding. Department of Science and Technology, Ministry of Science and Technology, India (DST/NM/TUE/QM-1/2019, DST/TDT/AMT/2021/003 (G)&(C)); Ministero dell'Università e della Ricerca (CUP B53C22001750006, ID D2B8D520, I-PHOQS, IR0000016); HORIZON EUROPE European Innovation Council (101130384, HORIZON-EIC-2023-PATHFINDEROPEN-01, QUONDENSATE, 101047137, HORIZON-EIC-2021-PATHFINDEROPEN-01, TROPHY); HORIZON EUROPE Marie Skłodowska-Curie Actions (812992, MUSIQ).

Disclosures. The authors declare no conflicts of interest.

Data availability. Data underlying the results presented in this paper are available in Ref. [38].

Supplemental document. See [Supplement 1](#) for supporting content.

References

1. G. Piland and E. M. Grumstrup, “High-repetition rate broadband pump-probe microscopy,” *J. Phys. Chem. A* **123**(40), 8709–8716 (2019).
2. L. Wei and W. Min, “Pump-probe optical microscopy for imaging nonfluorescent chromophores,” *Anal. Bioanal. Chem.* **403**(8), 2197–2202 (2012).
3. Z. Guo, Y. Wan, M. Yang, *et al.*, “Long-range hot-carrier transport in hybrid perovskites visualized by ultrafast microscopy,” *Science* **356**(6333), 59–62 (2017).

4. M. Delor, H. L. Weaver, Q. Q. Yu, *et al.*, “Imaging material functionality through three-dimensional nanoscale tracking of energy flow,” *Nat. Mater.* **19**(1), 56–62 (2020).
5. J. Sung, S. Macpherson, and A. Rao, “Enhanced ballistic transport of charge carriers in alloyed and K-passivated alloyed perovskite thin films,” *J. Phys. Chem. Lett.* **11**(14), 5402–5406 (2020).
6. H. L. Weaver, C. M. Went, J. Wong, *et al.*, “Detecting, distinguishing, and spatiotemporally tracking photogenerated charge and heat at the nanoscale,” *ACS Nano* **17**(19), 19011–19021 (2023).
7. M. M. Gabriel, J. R. Kirschbrown, J. D. Christesen, *et al.*, “Direct imaging of free carrier and trap carrier motion in silicon nanowires by spatially-separated femtosecond pump-probe microscopy,” *Nano Lett.* **13**(3), 1336–1340 (2013).
8. E. Ploetz, S. Laimgruber, S. Berner, *et al.*, “Femtosecond stimulated Raman microscopy,” *Appl. Phys. B* **87**(3), 389–393 (2007).
9. C. W. Freuding, W. Min, B. G. Saar, *et al.*, “Label-free biomedical imaging with high sensitivity by stimulated raman scattering microscopy,” *Science* **322**(5909), 1857–1861 (2008).
10. F. Hu, L. Shi, and W. Min, “Biological imaging of chemical bonds by stimulated Raman scattering microscopy,” *Nat. Methods* **16**(9), 830–842 (2019).
11. S. Adhikari, P. Spaeth, A. Kar, *et al.*, “Photothermal microscopy: imaging the optical absorption of single nanoparticles and single molecules,” *ACS Nano* **14**(12), 16414–16445 (2020).
12. D. Zhang, L. Lan, Y. Bai, *et al.*, “Bond-selective transient phase imaging via sensing of the infrared photothermal effect,” *Light: Sci. Appl.* **8**(1), 116 (2019).
13. K. Kniazev, E. Zaitsev, S. Zhang, *et al.*, “Hyperspectral and nanosecond temporal resolution widefield infrared photothermal heterodyne imaging,” *ACS Photonics* **10**(8), 2854–2860 (2023).
14. R. Vanna, A. De la Cadena, B. Talone, *et al.*, “Vibrational imaging for label-free cancer diagnosis and classification,” *Riv. Nuovo Cim.* **45**(2), 107–187 (2022).
15. K. C. Robben and C. M. Cheatum, “Edge-pixel referencing suppresses correlated baseline noise in heterodyned spectroscopies,” *J. Chem. Phys.* **152**(9), 094201 (2020).
16. F. Kanal, S. Keiber, R. Eck, *et al.*, “100-kHz shot-to-shot broadband data acquisition for high-repetition-rate pump-probe spectroscopy,” *Opt. Express* **22**(14), 16965 (2014).
17. N. M. Kearns, R. D. Mehlenbacher, A. C. Jones, *et al.*, “Broadband 2D electronic spectrometer using white light and pulse shaping: noise and signal evaluation at 1 and 100 kHz,” *Opt. Express* **25**(7), 7869 (2017).
18. K. L. Haller and P. C. D. Hobbs, “Double-beam laser absorption spectroscopy: shot noise-limited performance at baseband with a novel electronic noise canceler,” in *Optical Methods for Ultrasensitive Detection and Analysis: Techniques and Applications* (SPIE, 1991), 1435, pp. 298–309.
19. C. Schriever, S. Lochbrunner, E. Riedle, *et al.*, “Ultrasensitive ultraviolet-visible 20 fs absorption spectroscopy of low vapor pressure molecules in the gas phase,” *Rev. Sci. Instrum.* **79**(1), 013107 (2008).
20. F. Crisafi, V. Kumar, T. Scopigno, *et al.*, “In-line balanced detection stimulated Raman scattering microscopy,” *Sci. Rep.* **7**(1), 10745 (2017).
21. S. A. Crooker, D. D. Awschalom, and N. Samarth, “Time-resolved faraday rotation spectroscopy of spin dynamics in digital magnetic heterostructures,” *IEEE J. Sel. Top. Quantum Electron.* **1**(4), 1082–1092 (1995).
22. A. L. Dobryakov, S. A. Kovalenko, A. Weigel, *et al.*, “Femtosecond pump/supercontinuum-probe spectroscopy: Optimized setup and signal analysis for single-shot spectral referencing,” *Rev. Sci. Instrum.* **81**(11), 113106 (2010).
23. J. Brazard, L. A. Bizimana, and D. B. Turner, “Accurate convergence of transient-absorption spectra using pulsed lasers,” *Rev. Sci. Instrum.* **86**(5), 053106 (2015).
24. E. M. Fantuzzi, S. Heuke, S. Labouesse, *et al.*, “Wide-field coherent anti-Stokes Raman scattering microscopy using random illuminations,” *Nat. Photonics* **17**(12), 1097–1104 (2023).
25. M. Liebel, F. V. A. Camargo, G. Cerullo, *et al.*, “Ultrafast transient holographic microscopy,” *Nano Lett.* **21**(4), 1666–1671 (2021).
26. M. Hörmann, F. Visentin, A. Zanetta, *et al.*, “High-sensitivity visualization of ultrafast carrier diffusion by wide-field holographic microscopy,” *Ultrafast Sci.* **3**, 0032 (2023).
27. European Machine Vision Association, “EMVA Standard 1288 - 3.0: Standard for characterization of Image Sensors and Cameras,” (2012).
28. J. R. Janesick, *Photon Transfer* (SPIE press, 2007), (PM170).
29. B. Lang, “Photometrics of ultrafast and fast broadband electronic transient absorption spectroscopy: State of the art,” *Rev. Sci. Instrum.* **89**(9), 093112 (2018).
30. Y. Feng, I. Vinogradov, and N.-H. Ge, “General noise suppression scheme with reference detection in heterodyne nonlinear spectroscopy,” *Opt. Express* **25**(21), 26262 (2017).
31. D. Polli, L. Lüer, and G. Cerullo, “High-time-resolution pump-probe system with broadband detection for the study of time-domain vibrational dynamics,” *Rev. Sci. Instrum.* **78**(10), 103108 (2007).
32. P. K. Sahoo, S. Memaran, Y. Xin, *et al.*, “One-pot growth of two-dimensional lateral heterostructures via sequential edge-epitaxy,” *Nature* **553**(7686), 63–67 (2018).
33. S. Dal Conte, C. Trovatiello, C. Gadermaier, *et al.*, “Ultrafast photophysics of 2D semiconductors and related heterostructures,” *Trends Chem.* **2**(1), 28–42 (2020).
34. C. Trovatiello, F. Katsch, N. J. Borys, *et al.*, “The ultrafast onset of exciton formation in 2D semiconductors,” *Nat. Commun.* **11**(1), 5277 (2020).

35. Z. Wang, P. Altmann, C. Gadermaier, *et al.*, “Phonon-mediated interlayer charge separation and recombination in a MoSe₂/WSe₂ heterostructure,” *Nano Lett.* **21**(5), 2165–2173 (2021).
36. G. Bressan, I. Heisler, G. Greetham, *et al.*, “Half-broadband two-dimensional electronic spectroscopy with active noise reduction,” *Opt. Express* **31**(25), 42687–42700 (2023).
37. R. Pandya, R. Y. S. Chen, Q. Gu, *et al.*, “Femtosecond transient absorption microscopy of singlet exciton motion in side-chain engineered perylene-diimide thin films,” *J. Phys. Chem. A* **124**(13), 2721–2730 (2020).
38. M. Hörmann, F. Visentin, S. K. Chakraborty, *et al.*, “Self-referencing for quasi shot-noise-limited widefield transient microscopy,” Zenodo Version 1.0, 2024, <https://doi.org/10.5281/zenodo.11108136>